CIRP Journal of Manufacturing Science and Technology 65 (2026) 163–178

Contents lists available at ScienceDirect

CIRP Journal of Manufacturing Science and Technology

journal homepage: www.elsevier.com/locate/cirpj

A grey-box approach based on Johnson-Cook constitutive model to improve predictions of mechanical loads of cutting simulations for normalized AISI 1045

Jan Wolf [a,*], Erik Krumme [b], Nithin Kumar Bandaru [c], Martin Dienwiebel [c,d], Andreas Zabel [b], Hans-Christian Möhring [a]

[a] Institute for Machine Tools (IfW), University of Stuttgart, Holzgartenstraße 17, Stuttgart 70174, Germany
[b] Institute of Machining Technology (ISF), TU Dortmund University, Baroper Straße 303, Dortmund 44227, Germany
[c] Institute for Applied Materials (IAM), Microtribology Center μTC, Karlsruhe Institute of Technology, Straße am Forum 5, Karlsruhe 76131, Germany
[d] Fraunhofer Institute for Mechanics of Materials (IWM), Wöhlerstraße 11, Freiburg 79108, Germany

ARTICLE INFO

Keywords:
Grey-box model
Force prediction
Johnson-Cook constitutive model
FEA

ABSTRACT

In machining, high temperatures and strain rates impact the flow stress of the workpiece material, making it essential to understand the materials behaviour in these process conditions for meaningful finite element analysis (FEA) of the cutting process. The Johnson-Cook constitutive model, despite being the most widely applied, is reported to struggle in capturing the material behaviour outside of the reference conditions it was calibrated on. However determining these parameters in conventional material tests is challenging. To solve this issue, this study proposes a grey-box approach which aims to increase the accuracy of process force prediction of FEA, employing a Johnson-Cook model determined by experiments conducted on a Split-Hopkins Pressure Bar and compression tests at elevated temperatures on a Gleeble 3800c for AISI 1045, over a variety of cutting parameters. In total 110 cutting experiments and their corresponding simulations were carried out in a fully factorial experimental design with eleven cutting speeds and ten uncut chip thicknesses. Succeeding the white-box model, a black box model is trained to capture the non-linear behaviour between the simulation and the cutting experiments. Among the tested algorithms, XGBoost and Support Vector Regression outperformed Random Forests and Neural Network for predicting cutting force and feed force. The proposed grey-box approach showed an improved capability of predicting cutting force and feed force, reducing the mean absolute error and mean squared error compared to the white-box model by 97.9 % and 99.9 % for cutting force and by 94.9 % and 99.7 % for feed force, respectively. The grey-box model achieved a mean error of 1.3 % with a standard deviation of 0.1 in process force prediction.

1. Introduction

Machining contributes to 5 % of the GDP of developed countries and translates into yearly $250B in the U.S [1]. . In order to increase the productivity and sustainability of the machining processes, finite element analysis (FEA) has become an increasingly important tool due to the ever-increasing performance of computers and the resulting increase in simulation results accuracy and the possibility to integrate more features e.g. for tool wear [2]. Examples are the identification of improved process parameters and improved tool geometries [3] and thus contributed to reducing manufacturing costs [4]. FEA helped significantly to understand the complex physical and mechanical interactions between the tool, the machined material and the chip [5]. As the complexity of machining in the simulation is time-consuming and cost-intensive, for example in milling, the machining case is usually simplified to the orthogonal cut [6]. With this approach, complex machining operations can be modelled in 2D which leads to a significant reduction of required computational resources compared to 3D simulations. Thus, orthogonal cutting is the basis of many studies conducted on simulating milling [7], drilling [5] and lathe [8]. To setup the FEA different forms of meshing are used which includes Eulerian,

Lagrangian and Arbitrary Lagrangian-Eulerian (ALE). Most FE

* Corresponding author.
E-mail address: jan.wolf@ifw.uni-stuttgart.de (J. Wolf).

https://doi.org/10.1016/j.cirpj.2025.12.014
Received 17 February 2025; Received in revised form 17 December 2025; Accepted 21 December 2025
Available online 7 January 2026

Table 1
Chemical composition of normalized AISI 1045 in accordance with DIN EN ISO 683–1.

C	Si	Mn	P	S	Cr	Mo	Ni	Al	Cu
0.431	0.233	0.653	0.011	0.024	0.124	0.005	0.018	0.029	0.029

software systems use a 2D Lagrangian mesh formulation, which requires constant remeshing [9]. The tool is commonly modelled as a rigid body [10] which results in an efficient simulation since the nodes of the tool are not displaced [11]. Since machining is a highly nonlinear, coupled thermo-mechanical dynamic process, the result of an FEA simulation depends mainly on the friction, mechanical and thermal loads, chip formation and material flow models [6]. Multiple approaches exist in some category, whereby the appropriate model must be selected depending on the application. Therefore, expertise is required to apply the right models. Regarding wear e.g. the Usui model [12] is regularly used to predict the wear rate, however different models such as Archard or Arrhenius-style equations exist that may be used depending on the prevailing wear mechanism. As tool wear is mainly influenced by the workpiece material behaviour, material modelling also is of great significance. The introduction of constitutive equations, which are a mathematical representation of the flow behaviour of materials [13] are a vital part to achieve meaningful machining simulations [14,15]. As a result, material characterization for determination of material models received increasing attention [16]. Constitutive models can be divided into three categories which are empirical e.g. Johnson Cook (J-C) and Zerilli-Armstrong (Z-A) [17], phenomenological and physical models e.g. mechanical threshold stress and Bammann-Chiesa-Johnson [18]. The main flow stress models for AISI 1045 are J-C, Z-A, Oxley, Maekawa and El-Magd constitutive models [19]. Additional models such as the Bodner Partom model which was found to model the behaviour of a rate sensitive metal for different tensile straining histories [20] were developed. However, the focus of this study lies on the J-C constitutive model due to their proven accuracy and simple forms [18].

The J-C model [21] is the most widespread to model machining operations and relates flow stress with strain, strain-rate and temperature [22]. It was successfully applied in multiple studies regarding linear friction welding processes [23], selective laser melting [24] and machining [25,26]. Eq. (1) explains the J-C model where σ is the flow stress, ε_p is the effective plastic strain, $\dot{\varepsilon_p}$ is the plastic strain rate, $\dot{\varepsilon_0}$ is the reference strain rate while T, T_m and T_0 are the test temperature, the melting point of the material and the reference temperature, respectively [27]. As a result A, B, C, n and m are the material-dependent parameters [22] where A is the initial yield stress at reference strain rate and temperature, B is the hardening modulus, C is the strain rate dependency coefficient, n is the work hardening exponent and m is the thermal softening component [28]. From the equation it can be derived that the J-C model contains three parts which are the strain hardening, strain rate and thermal softening [29]. To obtain meaningful parameters the material should be tested at conditions which occur in the actual machining process. During machining high strain rates of up to 10^6 s^{-1} and temperatures of up to 1200°C occur which are difficult to obtain through conventional tensile or compression test [15]. These parameters are difficult to reach in material testing experiments. This explains why several researchers utilized a Split Hopkins Pressure Bar (SHPB) that, depending on the setup, can reach strain rates of 10^5 -10^6 s^{-1}.

$$\sigma = (A + B\varepsilon_p^n)\left[1 + C\ln\left(\frac{\dot{\varepsilon_p}}{\dot{\varepsilon_0}}\right)\right]\left[1 - \left(\frac{T - T_0}{T_m - T_0}\right)^m\right] \quad (1)$$

In general, there are two approaches to determine the parameters of the J-C material models for the modelling of machining operations [30]. The first approach is to conduct material testing experiments such as SHPB tests, tensile and compression tests as conducted by [31]. In the latter case, quasi-static experiments at low strain rates and different temperatures are performed. Subsequently, mathematical methods are applied to determine the J-C parameters [32]. As a second approach, the J-C parameters can be determined inversely by matching machining experiments to the simulation model while changing the parameters to iteratively achieve a better fitting. Methods such as artificial intelligence and different optimization algorithms e.g. particle swarm optimization [22] were applied to solve the multi-dimensional optimization problem. However, the second approach comes with the downside of a non-uniqueness of the J-C parameter set and usually only applies to a limited parameter range.

Besides its simplicity, some researchers criticize the J-C model. As pointed out by [33], at high temperatures and non-linear flow stress behaviour connections between i.e. strain, strain rate and temperature exist which is not modelled by Eq. (1). That is why several researchers focused on optimizing the J-C model to improve the prediction of the flow stress behaviour and focused on a different constitutive model. With the goal of providing adjusted constitutive models for specific materials and processes, modified J-C models were developed.

Despite some criticism, the J-C model was found to model material flow better than the Z-A model at strain rates up to 5000 s^{-1} and temperatures up to 1000°C [19].

In addition, an inverse determination of J-C constants for AISI 1045 was carried out and validated through a comparison of experimental and simulated cutting [34]. Therefore, it can be concluded that the original Johnson-Cook model is well suited to describe the flow behaviour of AISI 1045. Even though many researchers focused on the determination of suitable material models for meaningful cutting simulations, discrepancies between measured and simulated cutting conditions still exist and are obvious when applying the model to a wide range of cutting parameters such as cutting depth and velocity. To overcome this shortcoming and to improve the prediction capabilities of mechanical loads in FEA, this study focuses on the determination of a grey-box model to address those discrepancies. The applied methods to build this model are described in chapter 2.

2. Experimental setups

This study utilizes normalized AISI 1045. With respect to DIN EN ISO 683–1 the data in Table 1 has been collected. Furthermore, the grain size is greater or equal to 5 μm with respect to DIN EN ISO 643 and the Brinell hardness ranges from 178 to 180 HBW with respect to DIN EN ISO 6506.

2.1. Experimental determination of J-C parameters

For the experimental determination of the J-C parameters two setups where utilized. To determine the constant C a Split-Hopkins-Pressure-Bar (SHPB) was used. Since its introduction of SHPB in the early twentieth century, it is widely applied for testing materials at high strain rates [35]. While contactless methods of material testing are available, the SHPB has stood the test of time and continues to be widely used [36]. Basically, the test setup consists of a projectile, an input rod, an output rod and the material sample, which are all aligned concentrically to each other. The rods should have a length-to-diameter ratio of at least l/D $>$ 20 in order to ensure one-dimensional wave propagation [36]. As a general practice, ratios of l/D $>$ 100 can be found [37]. The material sample is positioned between the input and output bars. A strain gauge is attached to the centre of both rods. The projectile is accelerated using a pulse generator, which is usually pneumatically operated, and hits the input rod. When the projectile hits the input rod, a longitudinal pressure wave is generated in both components, which propagates axially. As the

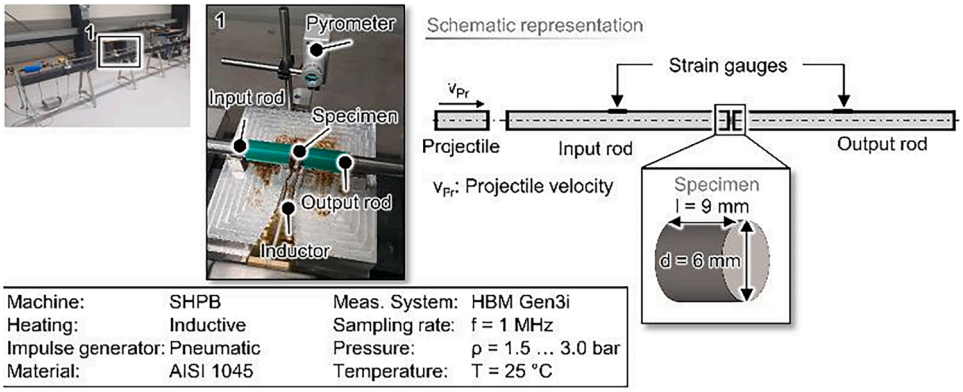

Fig. 1. Schematic overview of the Split Hopkinson Pressure Bar utilized at ISF.

projectile is considerably shorter than the rods, the pressure wave is initially reflected as a tensile wave at the free end of the projectile. During the time that the projectile is in contact with the input rod, a pulse is initiated which is recorded using the strain gauge. Once the wave in the input rod reaches the interface with the material sample, the impedance difference, partial reflection and transmission occurs. The transmitted pulse is also recorded using a strain gauge on the output rod. The strain measurements are then used to calculate the strain and strain rate as well as the stress of the sample [38].

Assuming that the forces at the contact points between the specimen and the rods are equal and taking into account the superposition of the incoming and reflected wave, the strain rate and the stress of the specimen are obtained as a function of the reflected and transmitted rod strain ε_r and ε_a respectively. The strain φ_P results from the temporal

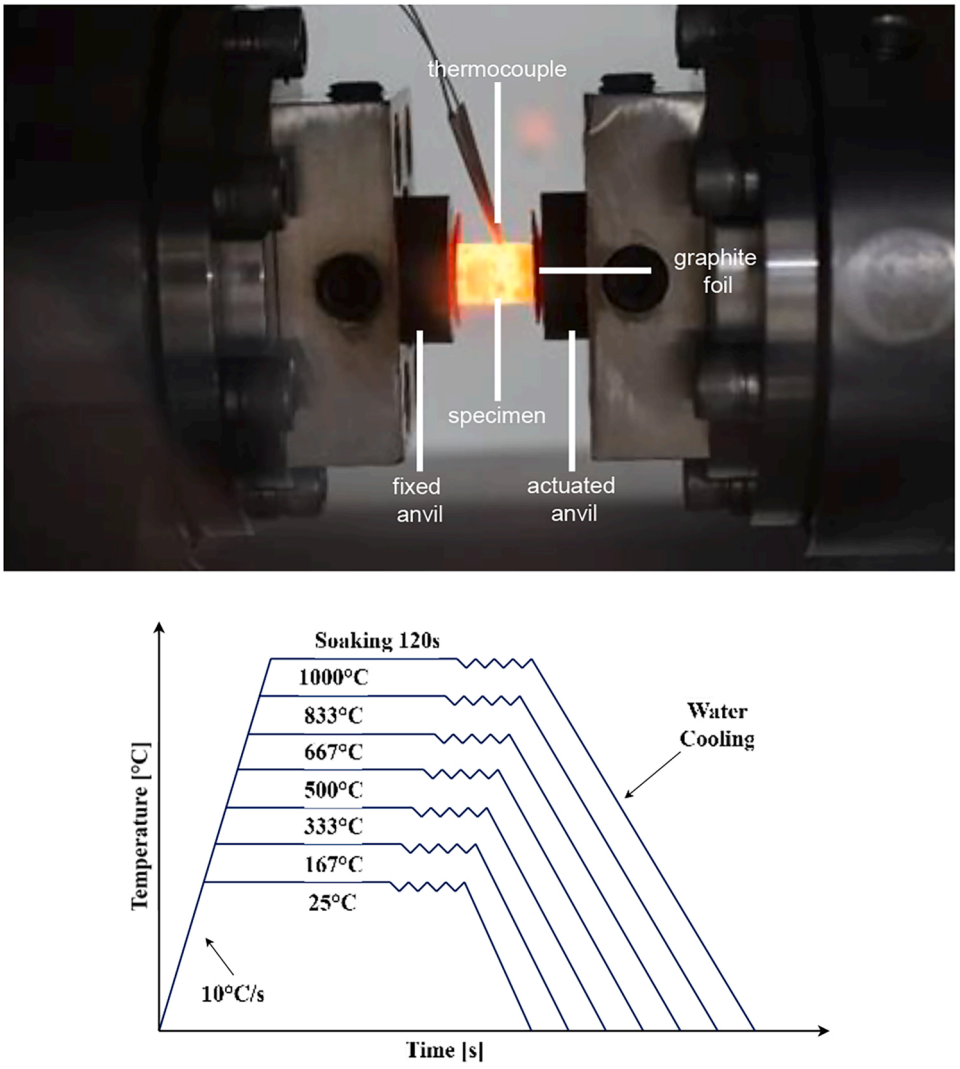

Fig. 2. Gleeble 3800c apparatus (top) and experimental design for different temperature conditions (bottom).

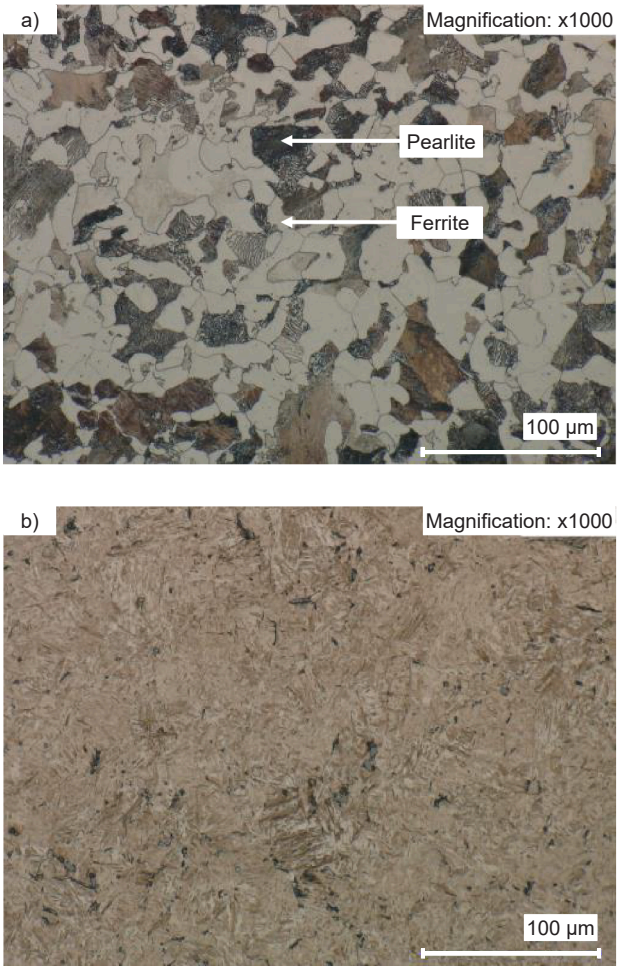

Fig. 3. Grain structure of the AISI 1045 at 25°C (a) and after heating to 1000°C and compression (b).

integration of the strain rate

The following equations can thus be given for the stress, strain rate and strain [38]:

$$\sigma_P = \frac{A_{rod}E_{rod}}{A_P}\varepsilon_a \tag{2}$$

$$\dot{\varphi}_P = \frac{2c_s}{l_p}\varepsilon_r \tag{3}$$

$$\varphi_P = \frac{2c_s}{l_p}\int_0^t \varepsilon_r \tag{4}$$

The SHPB test rig used to determine parameter C has a length of approx. 8 m, whereby the impulse is initiated by a precision pressure regulator in combination with an accelerated projectile. The input and output rods used are made of X37CrMoV5–1 hot-work tool steel and have a ratio of l/D = 107. The cylindrical test specimens diameter and length is 6 mm and 9 mm respectively with a maximum deviation of 0.02 mm. In order to ensure a valid measurement of the flow stress behaviour, the samples were ground plane-parallel and measured beforehand. Due to the high wave propagation speed of c = 5231 m/s, an HBM Gen3i data encoder with a sampling rate of f = 1 MHz was used. Within the work presented, the strain rates, indirectly adjusted by pressures of ρ = 1.5 … 3.0 bar, are investigated at room temperature. At least one test repetition was carried out per pressure level to statistically validate the results. The above equations were used to evaluate the recorded pulses from the strain gauges, allowing a stress-strain diagram and the strain rate to be determined. The test setup is shown in Fig. 1.

For determination of the thermal softening component *m* quasi static experiments have to be conducted at room temperature and at high temperatures. To achieve this, compression experiments are carried out with a Gleeble 3800c at temperatures of 25°C to 1000°C with an interval of 167°C. The strain rate is kept at a minimum of $4*10^{-3}$ s^{-1}. Test specimens are in a cylindrical shape with the length of 15 mm and diameter of 10 mm. A common tolerance for specimens is a maximum deviation of 0.02 mm. The front face's centre roughness value R_a is 0.4 µm while the lateral surface area's R_a is 0.8 µm. The setup is shown in Fig. 2 (top). The experimental procedure is as follows: First the specimens were heated to target temperature with an increase in temperature of 10°C s^{-1}. After the target temperature is reached, the heating phase is followed by a delay of 120 s which ensures a uniform temperature in the specimen [39].

Thereafter, the compression tests were performed during which the load and positional displacement are recorded.

Finally, the specimens are rapidly cooled to keep the grain structure. This experimental procedure is shown in Fig. 2 (bottom).

To analyse the microstructural evolution of AISI 1045 steel from its initial state to its compressed state at elevated temperatures of 833°C, a metallographic analysis was performed.

For sample preparation, each sample was sectioned at the centre, embedded in epoxy resin, and then subjected to subsequent grinding and polishing steps. Grinding was performed using silicon carbide (SiC) abrasive papers, from coarse (80 µm) to fine (2500 µm) grain papers. Polishing steps followed with finer grades, from 6 µm to 1 µm, to achieve

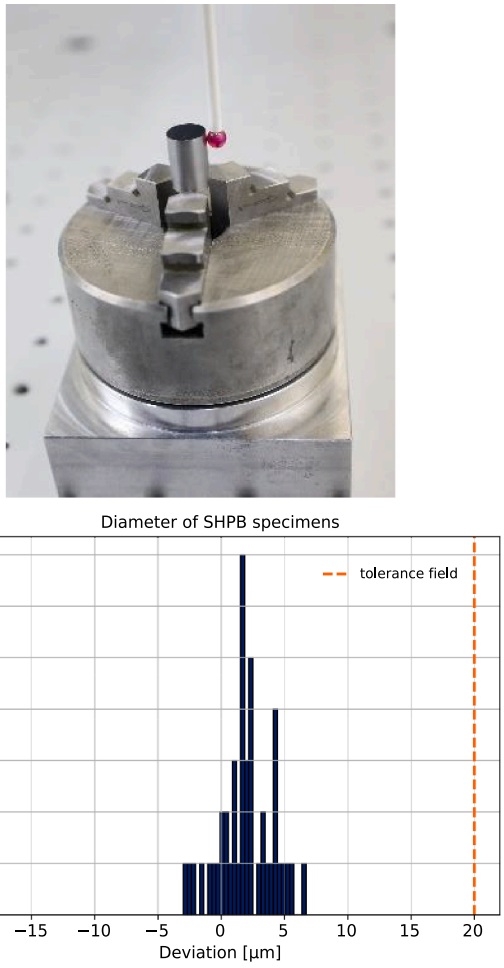

Fig. 4. Exemplary clamping of a specimen on a Wenzel LH 87 (top) and resulting measurement of diameter (bottom).

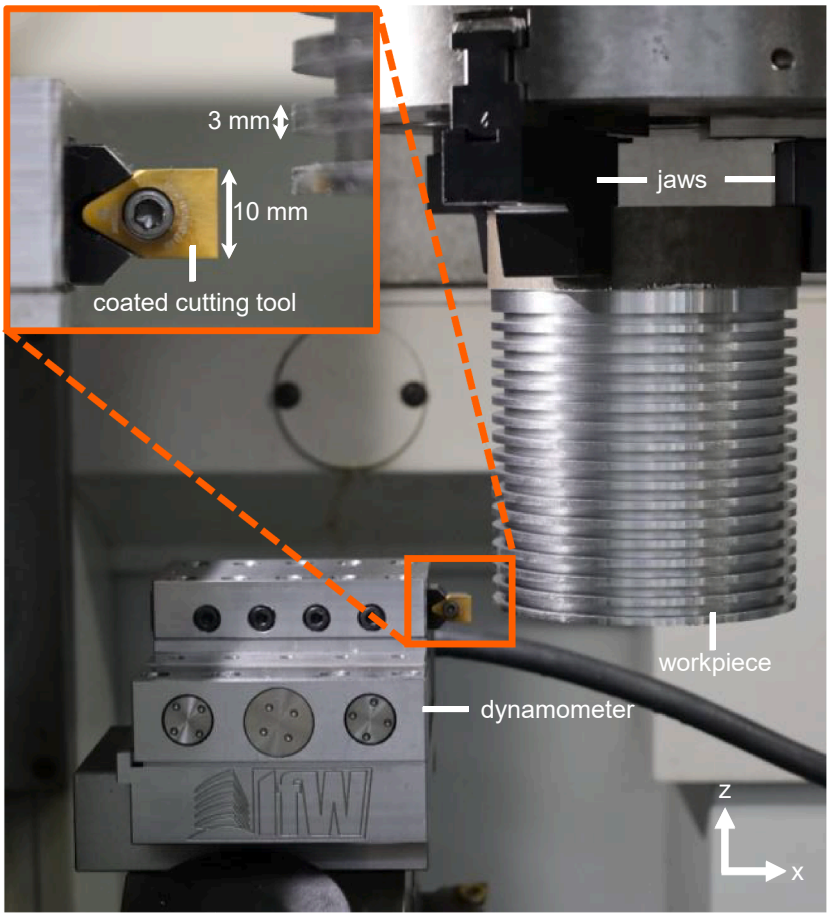

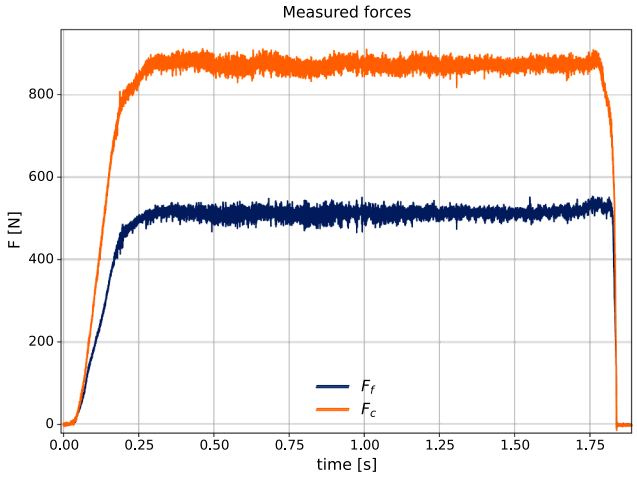

Fig. 5. Experimental setup for measurement of cutting and feed forces (top) and raw time series of measured forces (bottom).

a mirror-like finish. After each step, samples were cleaned with isopropylene and finally cleaned with ultrasonic isopropylene bath to remove any remaining contaminants. A final etching step with 5 % Nital was applied which was used to reveal the microstructural features characteristic of carbon steels. Microscopy was conducted using a Keyence VHX 650, with images captured at 1000x magnification using a 200x lens. Fig. 3 (top) illustrates the original grain boundaries and distinct

ferrite and pearlite colonies, whereas Fig. 3 (bottom) shows the microstructure that emerged following heating to 1000°C before compression. The darker structures in the images indicate regions of pearlite, characterized by alternating layers of ferrite. Compression at elevated temperatures is expected to have induced grain elongation along the compression axis, enhancing anisotropic properties in the material.

2.2. Specimen preparation

To account for manufacturing induced irregularities of the specimen sizes, they were measured by a coordinate measurement machine (CMM) LH 87 equipped with a PH10M plus head and a SM25–2 scanning module by Renishaw. To evaluate the dimensions the length and diameter were measured for all specimens used in the compression tests. This way the true stress σ_t and true strain ε_t according to Eq. (5) and

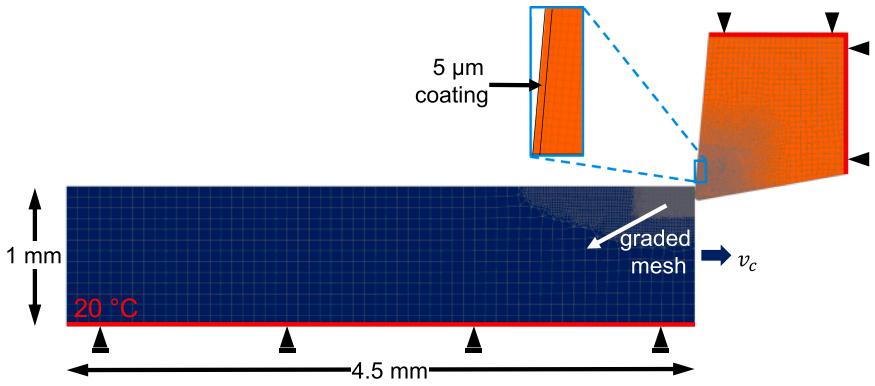

Fig. 6. Schematic of the chip formation model.

Eq. (6), where L_0 is the intial length and A_0 is the initial area can be calculated based on the measured load F and displacement ΔL whilst adjusting for the real dimensions at an accuracy down to the sub µm range.

$$\varepsilon_t = \ln(1 + \frac{-\Delta L}{L_0}) \tag{5}$$

$$\sigma_t = \frac{F}{A_0} e^{\varepsilon_t} \tag{6}$$

Prior to the measurements the CMM was referenced and the utilized ruby touch probe was calibrated on a ceramic reference sphere artefact. The setup is shown in Fig. 4.

2.3. Experimental validation of process forces determined by means of FEA

In order to validate the determined J-C parameters, machining experiments are carried out during which the cutting forces and feed forces are measured via a 9129 A dynamometer by Kistler. Subsequently these forces are compared with those predicted by FEA employing the determined J-C parameters. TiN/AlTiN coated cutting tools provided by Paul Horn GmbH were utilized for orthogonal turning with an unprofiled cutting edge on an EMAG VLC 250 vertical lathe machine. In total ten different uncut chip thicknesses between 0.06 mm and 0.15 mm with an interval of 0.01 mm paired with eleven cutting speeds between 100 m/min and 200 m/min with an interval of 10 m/min were recorded. The diameter of the workpiece is 118 mm which reduces the error made by the assumption of orthogonal cutting for comparison with the simulation. The experimental setup for measurement of forces is depicted in Fig. 5. Ploughing can be neglected, as the ratio of uncut chip thickness to cutting edge radius is 3, which is one order of magnitude larger than reported for AISI1045 [40].

By leveraging a 24 V output from the control unit, which was toggled between HIGH and LOW states through G-code commands within a programmed loop to trigger starting and stopping of force measurements, a fully automated measurement chain was established. A producer-consumer architecture implemented in LabVIEW enabled the automated logging of force measurements into uniquely labeled files corresponding to each parameter variation. These files were subsequently processed using a Python algorithm, which extracted the force data into a structured table. The entire cutting process was completed in under three minutes. Thanks to modern data acquisition techniques, both the collection and post-processing of experimental data were conducted with high efficiency providing applicability of the proposed grey-box approach. Tool wear was not taken into account because the overall cutting time was short. In this stage of the study no further input parameters were considered. However, the application of this approach to different tool geometries is possible by utilizing well known equations to estimate the dependency of tool geometry variations to omit the necessity of generating a new dataset for each tool geometry while keeping the workpiece material constant. Although the presented framework is shown by utilizing AISI1045, the approach can be followed for other workpiece materials as well, given that they are suitable for being described with the JC-model.

Table 2
FEA model input parameters for AISI1045.

Parameter	Value	Ref.
Youngs modulus [GPa]	E(T)	[42]
Density [kgm^{-3}]	7850	
Poisson ratio []	0.3	
Thermal conductivity [Wm^{-1}K^{-1}]	λ(T)	[42]
Specific heat capacity [J kg^{-1}K^{-1}]	c_p(T)	[42]

Table 3
FEA model input parameters for carbide.

Parameter	Value	Ref.
Thermal conductivity [Wm^{-1}K^{-1}]	λ(T)	[43]
Specific heat capacity [J kg^{-1}K^{-1}]	c_p(T)	[43]

Each parameter combination from the experiments mentioned above is simulated within the FEA software package DEFORM-2D (v. 13.1). A Lagrangian formulation with remeshing is adopted. Remeshing triggers were the interference depth of 0.0015 mm. Prior to the simulations a mesh sensitivity analysis was conducted which resulted in meshing the workpiece with 5000 elements with an element size of 6.6 µm. A hybrid friction model is implemented where a shear friction model with $m = 1$ is chosen for the sticking zone while a coulomb friction model is implemented in the sliding region with $\mu = 0.25$ [41]. Each cutting simulation was performed until the force steady-state was reached. Mesh windows for a graded mesh were utilized to improve the efficiency of the simulation. The inner mesh window has a length and height of 0.5 mm and 0.3 mm respectively. The size ratio of elements from inner to the middle mesh window and the middle to the outer mesh window is two. These windows were attached to the tool and thus resulted in a dynamic meshing of the workpiece in the are of interest over the entire simulation. A schematic of the setup is shown in Fig. 6. The rake angle and clearance angle of the tool is 5° and 7° respectively. The cutting edge

Table 4
FEA model input parameters for AlTiN coating.

Parameter	Value	Ref.
Thermal conductivity [Wm^{-1}K^{-1}]	4.64 + 0.00054 T	[44]
Specific heat [J kg^{-1}K^{-1}]	c_p(T)	[45]
Coating thickness [µm]	3	

radius is determined as 20 μm. These values were determined by measurements conducted on an Alicona G5 with 10x magnification.

The material data of AISI1045, carbide and the AlTiN coating is listed in Table 2, Table 3 and Table 4 respectively.

A 20°C thermal boundary condition was applied to a selected group of nodes of the workpiece and tool as depicted in Fig. 6 by the red line.

2.4. Grey-box modelling of process forces

Though advanced machinery and test setups to determine the Johnson-Cook parameters were utilized, it becomes obvious that despite being a well-recognized constitutive model, the force prediction via FEA is still prone to errors. Besides the inaccuracy of the J-C model another contributing effect is the modelling of friction which has an effect on the heat generated at the contact between the workpiece, especially the chip and the tool and thus interrelations between the thermal softening term of Eq. (1) and the friction model exist. Unfortunately friction in cutting is not completely understood [46]. To overcome these interdependencies, the authors utilize a grey-box modelling approach to enhance the capabilities of FEA to accurately predict the mechanical loads during cutting.

As stated in [47], grey-box models are a composition of theory-driven (white-box) models f_T and data-driven (black-box) models f_D. Grey-box models can be classified as serial models where the output of f_T is the input of f_D or vice versa or as parallel models [48]. In order to fulfil the task of predicting accurate forces, the serial approach made up of an initial theory-driven model succeeded by a data-driven model can be applied. In this architecture, the succeeding data-driven model applies minor adjustments to the theory-driven model's output which essentially comes down to a regression approach. Based on the mathematical explanation for the case of regression described in [47], an output $\boldsymbol{y}\in Y$ is predicted based on the input vector $\boldsymbol{x}\in X$ through the function G that takes the vector $\boldsymbol{x}$ as well as the functions f_T and f_D as an argument. This model can be described according to Eq. (7).

$$y(\boldsymbol{x}) = G(f_T, \quad f_D, \quad \boldsymbol{x}) \tag{7}$$

When considering the chosen structure of the grey-box model the function G essentially comes down to a sum operator. Concerning our application, $f_T(\boldsymbol{x})$ is the cutting/feed force output of the FEA model, y is the cutting/feed force determined via the experiments, $\boldsymbol{x}$ is the vector describing the cutting velocity and the cutting depth and $f_D(\boldsymbol{x})$ is the prediction of a data driven model employing artificial intelligence. Therefore, the training goal to enhance the force prediction with this grey-box architecture can be expressed with Eq. (8), where the loss function L is minimized through adjusting the trainable parameters of the black-box model Θ. A common loss function in regression is the mean squared error (MSE) across training samples n in Eq. (9), where y is the measured force and $\hat{y}$ is the sum of the predicted forces of the black-box and white-box model.

$$\min_{\Theta} L(y(v_c, \quad a_p), \quad (f_T(v_c, \quad a_p) + f_D(v_c, \quad a_p, \Theta))) \tag{8}$$

$$L(y, \hat{y}) = \frac{1}{n}\sum_{i=1}^{n}(y_i - \hat{y}_i)^2 \tag{9}$$

This grey-box model is inspired by two specific facts. Firstly, a limited amount of training data is necessary to achieve meaningful predictions, since basic knowledge of the materials behaviour is included in the white-box model. Furthermore, the complexity of the error defined by subtracting y and f_T is assumed to be reduced. Consequently, it is still beneficial to determine the J-C parameters and train a grey-box model over a sole black-box model, since basic explainability is obtained.

Besides choosing a suitable grey-box architecture, the artificial intelligence based model f_D for the regression has to be selected. Since one underlying idea of grey-box models is reducing the required training dataset size, the focus is put towards models which are known to work well with small datasets. In total, four models for f_T are studied which are random forest regression, support vector regression, extreme gradient boosting XGBoost and Neural Networks which have been utilized in previous studies by the authors on small datasets within the domain of cutting force prediction [49].

As a supervised machine learning algorithm proposed by Breimann [50], random forests are a scheme for building a predictor by a set of decision trees and is suitable for regression and classification [51]. Samples are drawn based on the bagging algorithm [50]. Since each tree's processing is done independently and is based on unique subsets of the training data, the algorithm has a limited risk of overfitting [52]. Random forest is considered a black-box model since it is hard to get insights from the prediction rule [53].

Support vector regression is a machine learning algorithm which offers robustness against outliers and is suitable for complex data. For the case of the accumulated dataset $D = \{(x_i, y_i)\}_{i=1}^{n} \in R^2 x R$ each training tuple is mapped into a feature space by the nonlinear function Φ where the linear function f is defined in accordance to Eq. (10) [54] with $\varphi(x)$ being a point in the feature space. Then w and b are determined by optimizing Eq. (11). SVR ensures that a function $f(x)$ with ε precision exists for the entire training dataset, where ε being equal to zero represents optimum regression [55]. Slack variables ξ_i, ξ_i^* are introduced to cope with infeasible constraints of the optimization problem while $J > 0$ defines the balance between the smoothness of f and the extent to which deviations beyond ε are accepted [56].

$$f(x) = \quad w^T\varphi(x) + b \quad , w \in \mathbb{R}^2 and b \in \mathbb{R} \tag{10}$$

$$\min \frac{1}{2}\|w\|^2 + J\sum_{i=1}^{n}(\xi_i + \xi_i^*)$$

$$\text{subject to} \begin{cases} y_i - w^T\varphi(x) - b \quad \leq \varepsilon + \xi_i \\ w^T\varphi(x) + b - y_i \leq \varepsilon + \xi_i^* \\ \xi_i, \quad \xi_i^* \geq 0 \end{cases} \tag{11}$$

Extreme Gradient Boosting (XGBoost) is a supervised machine learning system for tree boosting, where scalability is the main driver behind its success in addition to a ten times lower runtime compared to previous algorithms [57]. According to the nomenclature used in [58], an objective function which is the sum of a loss function L and a regularization term $\Omega(f_k)$ can be written as Eq. (12), where K represents the number of trees. With the number of leaves T, the score of the leave node w the regularization term can be written as Eq. (13).

$$obj = \quad \sum_{i=1}^{n} L(y_i, \hat{y}_i) + \sum_{k=1}^{K}\Omega(f_k) \tag{12}$$

$$\Omega(f_k) = \gamma T + \frac{1}{2}\lambda\sum_{j=1}^{T} w_j^2 \tag{13}$$

To guarantee an efficient use of XGBoost, the hyperparameters n_estimators, max_depth and learning_rate were systematically varied through a grid search with the best performing model being selected for evaluation. XGBoost is especially valuable for its ability to model nonlinear interactions between input parameters while at the same time offering interpretability through feature importance metrics. In this context, it allows for physical insights into how parameters such as cutting velocity and uncut chip thickness influence the simulations error of cutting/feed force, offering understanding beyond prediction accuracy.

As a last approach, a Feed Forward Neural Network (FFNN) is implemented. The basis of FFNN are perceptrons, which are connected to each other [49]. During training weights $\boldsymbol{w}_i$ with $i\in[1,n]$ are updated via backpropagation [59]. Non-linear behaviour is introduced via activation functions such as Rectified Linear Units (ReLU) in Eq. (14). When considering one neuron with input $\boldsymbol{x}_i$ and the bias b, the output y is calculated according to Eq. (15).

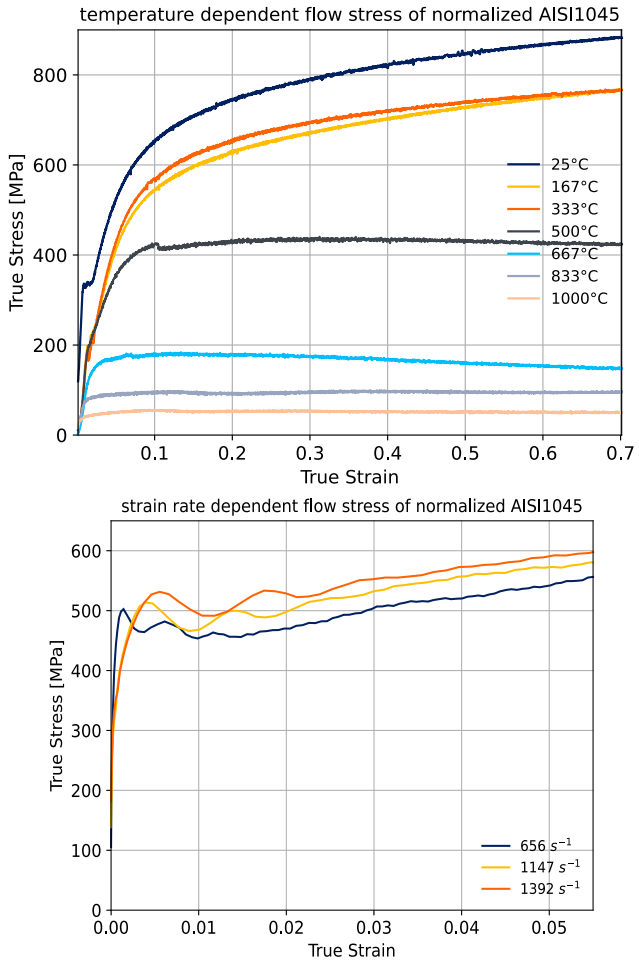

Fig. 7. Stress-strain curves measured with Gleeble 3800c (top) and SHPB (bottom).

$$y = ReLU\left(\sum_{i=1}^{n} \boldsymbol{w}_i \boldsymbol{x}_i + b\right) \tag{14}$$

$$\text{with} ReLU(x) = \begin{cases} x, \& x \geq 0 \\ 0, \& x < 0 \end{cases} \tag{15}$$

The chosen network structure consists of an input layer with two neurons. One is used for the cutting velocity and the other for the uncut chip thickness. Two hidden layers and an output layer with one neuron are trained. Only two hidden layers were chosen to keep the training parameters at a manageable range considering the size of the dataset. As a pre-processing step, the obtained data was standardized. Despite choosing a lean FFNN for a reduction of trainable features, the risk of overfitting is a valid concern for the model. This was countered by not only restricting the model complexity but also by using early stopping based on validation loss. To gain further insights in the models performance, a sobel sensitivity analysis is conducted, to quantify the effect of input features on the output of the neural network.In addition, 10 fold cross validation was performed, which is a resampling technique used to evaluate the generalization ability of the models. Averaging the performance across all folds enables the estimation of the models accuracy.

Table 5
J-C parameters for C45 determined by material testing.

A	B	n	C	m
331	614	0.26	0.07	1.19

Bootstrapping with 1000 iterations is introduced to all models to estimate the uncertainty of the applied metrics by sampling with replacement from the dataset.

When selecting AI approaches for regression tasks, it is argued that linear or polynomial regression models may outperform more complex methods when working with smaller datasets. For this reason, both linear regression and polynomial regression models of degree 2 and 4 were considered for a comparison in this study. While polynomial regression offers a more interpretable and theoretically grounded approach, higher-order models still require a substantial number of training data points. As highlighted in Eq. (16), the number of trainable features n depends on the degree of the polynomial g and the dimension of the input parameters d.

$$n = \binom{d+g}{g} \tag{16}$$

To ensure robust generalization, it is recommended that the size of the training dataset significantly exceed the number of trainable parameters. Under this point of view, the practical advantage of polynomial regression especially at higher orders diminishes when compared to the AI models presented in this work.

3. Results and discussion

3.1. Determined J-C Parameters

The stress strain curves resulting from compression tests are shown in Fig. 7 (top) and the stress-strain curves of the SHPB tests are shown in Fig. 7 (bottom).

When an experiment is performed at room temperature and at reference strain rate, the second and the third terms of Eq. (1) become 1 resulting in Eq. (17) which can be transferred into Eq. (18).

$$\sigma = (A + B\varepsilon_p^n) \tag{17}$$

$$\ln(\sigma - A) = \ln B + n\ln\varepsilon_p \tag{18}$$

The yield stress A can directly be obtained from the experimental results at reference temperature. This leaves two unknown parameters B and n from Eq. (4). This mathematical problem can be approached by linear regression when calculating ln(σ - A) over $\ln\varepsilon_p$ where n becomes the slope and B the offset [60]. Here, the least squares method is applied which minimizes the sum of squared residuals for each data point. Then Eq. (19) and Eq. (20) result for calculating n and B respectively.

$$n = \frac{\sum_{i=1}^{n}(x_i - \bar{x})(y_i - \bar{y})}{\sum_{i=1}^{n}(x_i - \bar{x})^2} \tag{19}$$

$$B = \bar{y} - n\bar{x} \tag{20}$$

Without considering thermal softening and therefore neglecting the stress strain curves from compression testing under temperatures unequal to room temperatures, Eq. (1) results in Eq. (21) which can be transferred to Eq. (22). By now, applying another linear regression the strain rate dependency coefficient C can be determined [61].

$$\sigma = (A + B\varepsilon_p^n)\left[1 + C\ln\left(\frac{\dot{\varepsilon}_p}{\dot{\varepsilon}_0}\right)\right] \tag{21}$$

$$\frac{\sigma}{A + B\varepsilon_p^n} = \left(1 + C\ln\left(\frac{\dot{\varepsilon}_p}{\dot{\varepsilon}_0}\right)\right) \tag{22}$$

At this point, the only unknown variable is the thermal softening component m. To determine m, the compression test results are evaluated. When these tests are performed at reference strain rate, Eq. (1) is simplified and can be written as Eq. (23), which is solved for m.

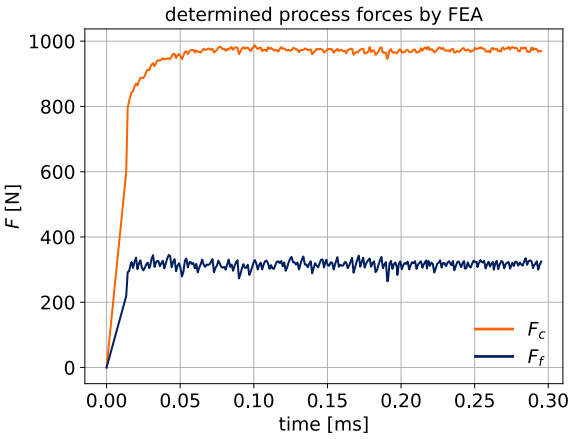

Fig. 8. Exemplary force signals for a 3 mm wide cutting edge at $v_c = 200$ m/min and $a_p = 0.1$ mm.

$$\sigma = \left(A + B\varepsilon_p^n\right)\left[1 - \left(\frac{T - T_0}{T_m - T_0}\right)^m\right] \tag{23}$$

As a result, the J-C parameters for AISI 1045 determined by material testing can be obtained from Table 5.

3.2. Comparison of measured and simulated process forces

For simulating orthogonal cutting of AISI 1045, the software DEFORM 3D V13.1 was used with the above determined J-C parameters values. A hybrid friction model based on Zorev with a coulomb friction factor μ= 0.25 [41] was chosen. The tool was modelled as rigid. Insights in the simulation and the resulting force can be determined from Fig. 8 for the cutting velocity 200 m/min and uncut chip thickness 0.1 mm.

The corresponding cutting experiments were conducted on an EMAG VLC250 vertical drilling machine. The dynamometer in use is a Kistler type 9129 A with a range of −10–10 kN and mounted on a custom made VDI40 tool holder. A multi-channel charge amplifier Kistler type 5080 was used. Lathe is a highly dynamical process which is why the dynamic behaviour of the dynamometer and the charge amplifier needs to be determined to allow for a reasonable measurement of the forces and the resulting evaluation of the measurements. Thus, an impact testing was performed in advance of the experiments to determine the frequency response function (FRF). Simcenter SCADAS by Siemens is used for this task where an impact hammer is chosen as the reference and the output of the charge amplifier is the input signal for determination of the FRF. The bandwidth and spectral lines are 3276.8 Hz and 2048 respectively, which leaves the acquisition as 0.625 s. The tip of the tool was chosen as the excitation point of the structure. The results of the analysis are shown in Fig. 9. Due to the acceptable setup of the measurement chain, measurement errors due to vibration were not considered in further evaluations.

The results of the cutting experiments as well as the simulations are shown in Fig. 10, where the cutting force F_c and the feed force F_f is represented by the z-axis.

The experimental results reveal that both forces increase with increasing cutting depth and slowly decrease with larger cutting velocities but the surfaces show nonlinear trends, especially in the feed force, where a sharp rise is observed at higher feed rates and lower cutting velocities. In contrast, the FEA results reproduce the general increase of forces with feed but display more linear surfaces and less variation dependend on the sliding velocity. This indicates that the determined J-C parameters do not fully capture the material behaviour in cutting processes. In addition, a strong force offset is noticeable for both directions. To further give insights into the dependence of cutting force and feed force on the cutting velocity and feed, the feed of 0.1 mm with variable cutting velocities and further the cutting velocity of 150 m/min with variable feed is selected for further evaluation and plotted in Fig. 11.

Here, it becomes clear that the trend of decreasing cutting force with increasing cutting velocity at a cutting depth of 0.1 mm was captured by the simulations, although not as pronounced as in the experiments. It remains difficult to attribute this trend to a single cause. However, the parameter C of the J-C model influences the flow stress with increasing cutting velocity, an effect that is superimposed by thermal effects and the parameter m, since higher cutting temperatures are generally observed with increasing cutting velocity. For a constant cutting velocity of 150 m/min, the cutting forces increase linearly in both the simulations and the experiments. When fitting a line via least squares through the cutting force values, the slope is determined as 8260 N/mm and 6318 N/mm for the simulations and the experiments respectively. A 23.5 % discrepancy in the slope values shows, that the error is not solely due to an initial offset of the values but rather arises from a complex combination of multiple influencing parameters. The underestimation of the feed force is a common phenomenon in metal cutting simulations and is not unique to this study. Despite good agreement at a cutting velocity of 150 m/min and a cutting depth of 0.06 mm, the simulation

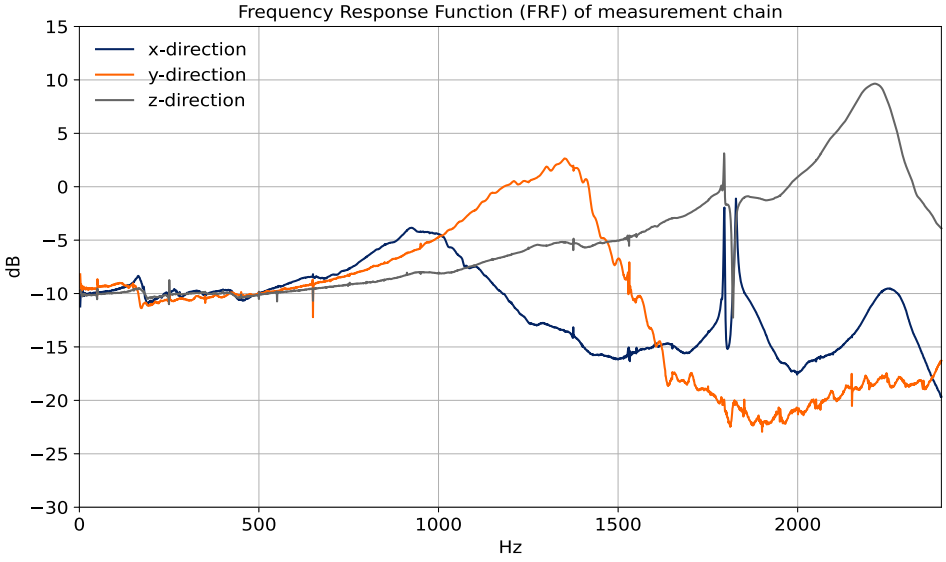

Fig. 9. FRF of the measurement chain containing the dynamometer and the charge amplifier.

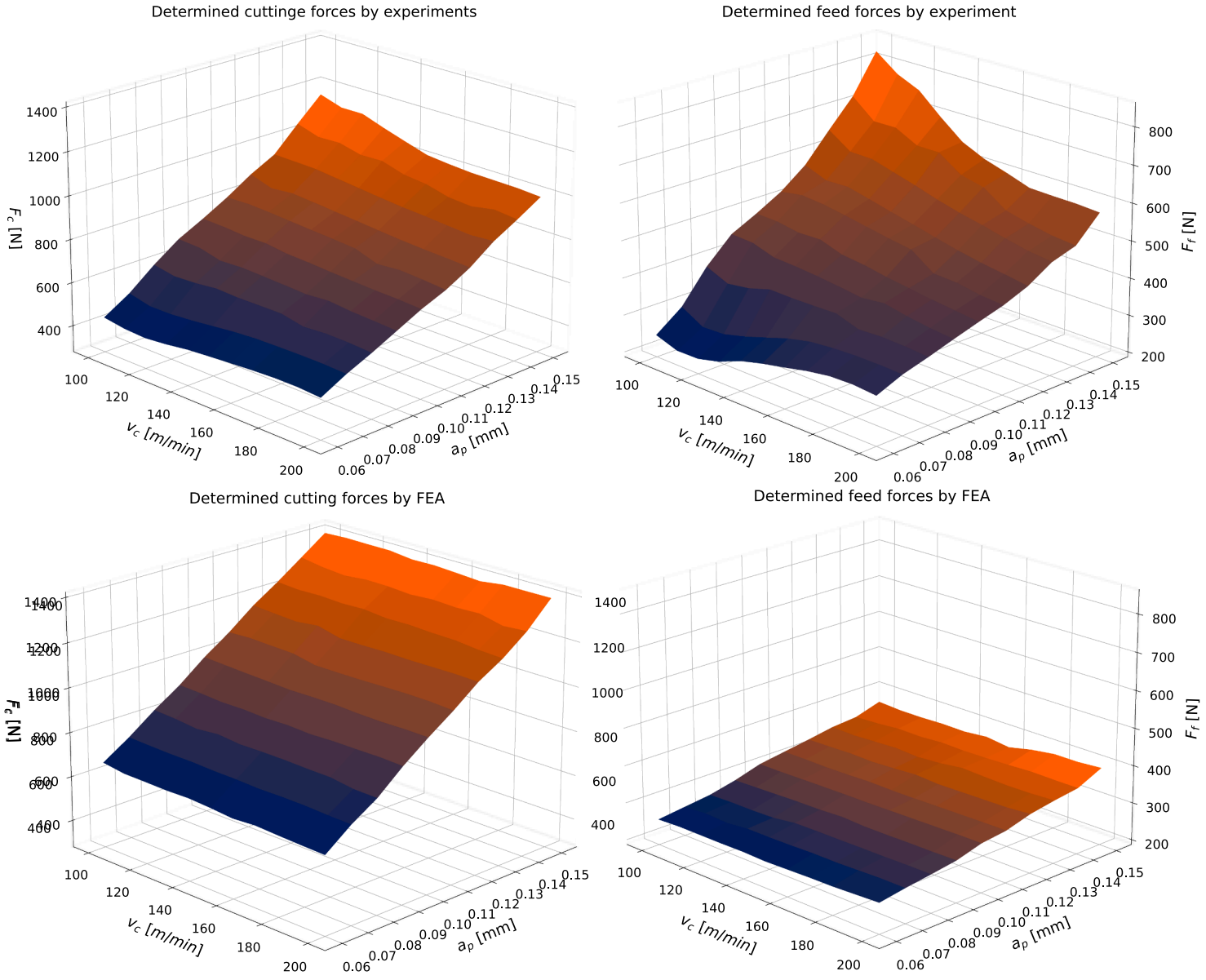

Fig. 10. Obtained cutting forces (top left) and feed forces (top right) by the cutting experiments and corresponding simulation results for cutting forces (bottom left) and feed forces (bottom right).

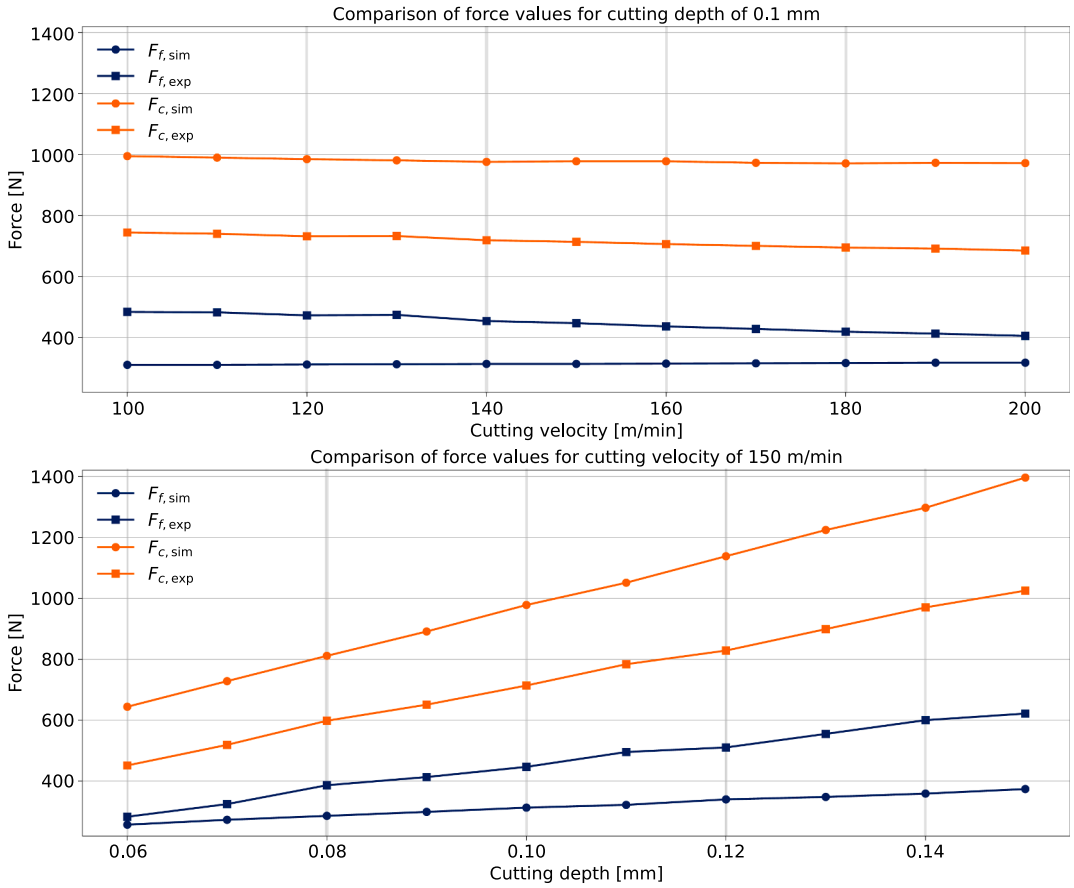

Fig. 11. Comparison of obtained forces for cutting depth of 0.1 mm (top) and cutting velocity 150 m/min (bottom).

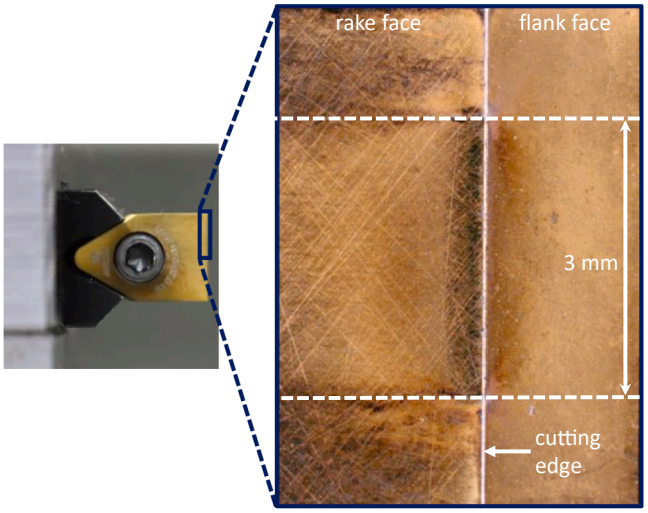

Fig. 12. Microscopic images of the cutting edge after conducting the experiments.

could not accurately capture the trend in feed force increase with higher cutting depths and the model did not register a decrease in feed force with higher cutting velocities. The later could be explained by the missing dependency of the coloumb friction coefficient on cutting velocity as studied in [62], where a lower friction coefficient is observed with increasing relative velocity which then results in lower process forces. This analysis is further supported by findings in [63], where simplified friction models and edge radius effects were identified as influencing factors for low feed forces in simulations. Despite having identified this influence, it remains an issue for future simulations due to missing available models for each coating and work matetrial combination.This again provides a foundation why grey-box modelling is a logical solution to tackle these

issues all at once in predicting accurate forces over a large range of cutting conditions. The error plot over all parameters is later shown in Fig. 13 onwards, as the difference of experimental and simulated values is depicted by the training and test data.

The geometry of the cutting insert was assessed after the cutting experiments to determine whether tool wear could have influenced the measured forces during the experiments. No noticeable changes in cutting edge radius exist. No coating delamination took place during the experiments, which could have potentially caused different friction properties, and thus cutting forces. Fig. 12 shows the cutting edge after conducting the experiments and underlines why tool wear is not considered in this study.

This leaves the difference between the plots in Fig. 10 to be captured by the Black-box models with a regression approach in accordance with the chosen grey-box architecture from chapter 2.4. Thus, the goal of the function f_D is to approximate these errors.

3.3. Evaluation of the proposed grey-box model

Given the results in Fig. 10, it is advantageous to apply regression algorithms that are able to capture the non-linear behaviour. The results of applying Support Vector Regression, Random Forest, Neural Networks and the XGBoost algorithm for this task is shown in Fig. 13. From the training data displayed in Fig. 13, the difference between simulation and experiments becomes clear.

From a first visual inspection, it can be concluded that all imple-

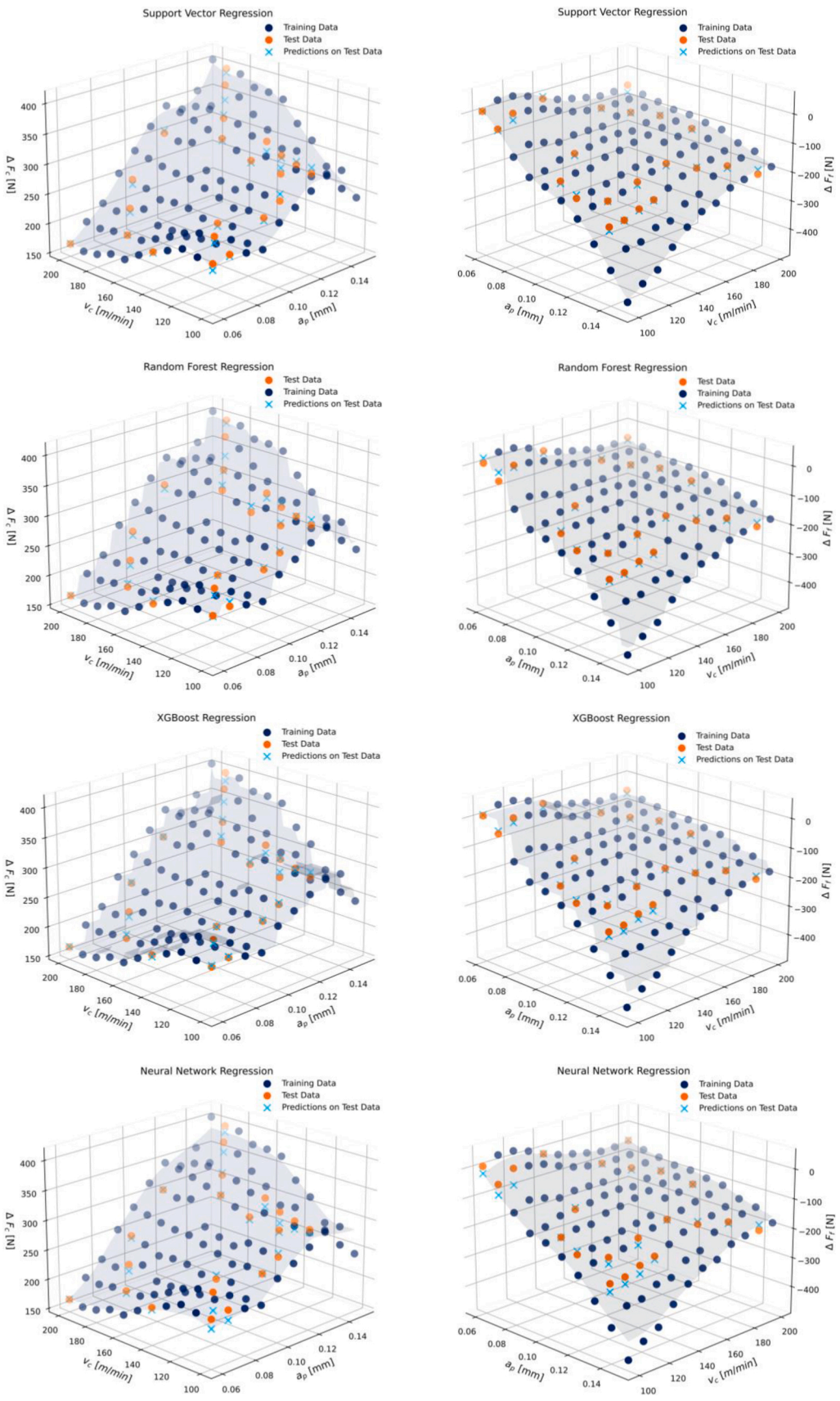

Fig. 13. Training results for the selected machine learning models for cutting force prediction (left) and feed force prediction (right).

Table 6
Evaluation metrics for implemented regression models with 95 % confidence intervals (CI).

			SV	RF	XG-Boost	FFNN	Lin. Reg.	Pol. Reg k = 2	Pol. Reg k = 4
MAE	μ	F_c	7.12	6.64	5.65	11.10	20.41	10.68	7.81
		F_f	7.60	8.01	9.03	13.85	30.72	12.84	9.85
	CI_-	F_c	4.97	4.43	3.62	9.04	13.84	8.03	5.12
		F_f	5.02	5.79	5.03	11.36	19.44	8.80	6.00
	CI_+	F_c	9.52	9.88	7.96	13.50	27.87	13.20	11.06
		F_f	10.86	10.70	10.54	16.63	43.58	17.37	14.24
MSE	μ	F_c	82.34	86.79	60.24	295.41	706.92	152.95	112.54
		F_f	104.65	96.24	116.07	512.87	1820.6	276.38	197.92
	CI_-	F_c	37.37	30.17	23.79	181.10	335.20	91.40	39.89
		F_f	40.46	43.11	63.39	287.13	776.77	130.84	63.09
	CI_+	F_c	146.06	187.34	104.56	450.76	1161.3	223.19	208.35
		F_f	186.22	177.14	176.06	787.62	3057.6	459.69	369.91
R^2		F_c	0.975	0.973	0.982	0.891	0.761	0.9472	0.961
		F_f	0.994	0.983	0.984	0.945	0.737	0.959	0.971
MAPE	μ	F_c	0.0246	0.023	0.0191	0.0403	0.0821	0.0394	0.0311
		F_f	0.38	0.2963	0.3502	0.2515	2.128	0.631	0.7351
	CI_-	F_c	0.0180	0.016	0.0133	0.0321	0.0517	0.0297	0.0188
		F_f	0.0402	0.0877	0.0669	0.0938	0.3692	0.082	0.0862
	CI_+	F_c	0.0317	0.031	0.0251	0.0490	0.1168	0.0492	0.0465
		F_f	0.9651	0.5698	0.7821	0.4532	4.9552	0.165	1.8246

Table 7
Results of sobel sensitivity analysis for neural network across 10 folds.

	$\mathbf{S1}\nu_c(\mu,\sigma)$	$\mathbf{S1}a_p(\mu,\sigma)$	$\mathbf{ST}\nu_c(\mu,\sigma)$	$\mathbf{ST}a_p(\mu,\sigma)$
F_c	0.874, 0.155	0.299, 0.056	0.411, 0.080	0.283, 0.076
F_f	0.794, 0.131	0.386, 0.069	0.376, 0.130	0.303, 0.076

mented machine-learning algorithms were able to capture the non-linear behaviour of the errors made by the FEA due to the algorithm's adaptability to the training data samples, which are displayed in dark blue. This is especially true for the region with low cutting depth and velocity. The fitting curve resulting from training is shown in each 3D plot. Notably the algorithms using tree-structures like XGBoost and Random Forest feature plateau like areas which centre around a training data sample. The SVR and Neural Network on the other hand feature a more consistent fitting curve. The feature importance calculation of XGBoost revealed 0.8682 / 0.7965 for ν_c and 0.2035/0.1318 for a_p depending on F_c / F_f.

The good approximation of the AI algorithms when it comes to unseen data is of great interest. The differences between the prediction on that data (blue crosses) and the true data (orange dots) is notable, although they mostly lie close together. When considering that a perfect model would lead to no discrepancy between the blue crosses and orange dots, a metric is necessary to capture the difference between them over the entire training dataset. To extract meaningful information over the regression capabilities of the different algorithms the metrics mean absolute error (MAE), mean squared error (MSE) and mean absolute percentage error (MAPE) are calculated and averaged over 1000 bootstrap resamples to provide insights in the variability of model performance due to random sampling. R^2 is given as point estimate. The results are listed in Table 6. For comparison, the MAE and MSE of the white-box model were 149.65 and 30748 for F_f and 272.31 and 77406 for F_c.

For MAE, XGBoost achieved the lowest values for F_c (5.65) while SVR outperformed all other models for F_p (7.60), indicating the most accurate predictions on average. RF also showed strong performance, with slightly higher MAE values, while FFNN and linear regression exhibited larger errors, particularly for F_f. The 95 % confidence intervals further indicate that XGBoost predictions are more stable for F_c, with narrower intervals compared to the other models.

In terms of MSE, XGBoost again showed the lowest error for F_c (60.24), though RF slightly outperformed it for F_f (96.24). FFNN and linear/polynomial regression had substantially higher MSE values, reflecting occasional large deviations from observed values. The confidence intervals confirm that XGBoost predictions are most reliable for F_c, whereas the other models lead to larger errors.

The R^2 values were generally high across most models, with XGBoost achieving 0.982 for F_c while SVR achieved 0.994 for F_f, indicating good regression capabilities. RF also performed well, while FFNN and linear/polynomial regression showed lower R^2 values.

Finally, MAPE results align with these findings. XGBoost had the lowest mean absolute percentage errors (0.0191 for F_c and 0.3502 for F_f), indicating the smallest relative errors. The other models show larger MAPE, reflecting less accurate predictions. MAPE values for F_f are consistently higher, as predictions near zero at low a_p inflate the relative error of individual cases and disproportionately affect the metric.

To further investigate the internal behaviour of the FFNN, a sobel sensitivity analysis was conducted, showing that the input variable ν_c accounted for the majority of the output variance.

For F_c, the variable ν_c shows the strongest first-order effect ($S1\nu_c$=0.874 ± 0.155), indicating that it explains the majority of the output variance on its own. In contrast, a_p has a relatively small first-order effect (STa_p=0.299 ± 0.056), suggesting it plays a secondary role. The total-order indices confirm this pattern: $ST\nu_c$= 0.411 ± 0.080 for ν_c and STa_p= 0.283 ± 0.076 for a_p. These values indicate that while a_p contributes some variance through interactions, the output is predominantly controlled by ν_c. For F_f, the importance of ν_c remains high

Table 8
Results of permutation for the trained models.

		SV	RF	XG-Boost	FFNN	Lin. Reg.	Pol. Reg k = 2	Pol. Reg k = 4
F_c	ν_c	0.0351	1.8520	1.8609	1.4333	1.5841	1.8276	1.8611
	a_p	0.0132	0.3355	0.3551	0.2276	0.0362	0.3691	0.3967
F_p	ν_c	0.0209	2.2742	2.2242	2.0384	1.6393	2.0918	2.1056
	a_p	0.0012	0.5282	0.5132	0.2980	0.1726	0.5880	0.6084

($S1v_c$=0.794 ± 0.131), though slightly reduced compared to F_c. The role of a_p is stronger than in the previous case ($S1a_p$=0.386 ± 0.069), reflecting a greater direct contribution. The total-order indices again show that interactions are small: STv_c= 0.376 ± 0.130 for v_c and STa_p= 0.303 ± 0.076 for a_p.

In this procedure, R^2 of the trained model is first computed. Then, for each feature, its values are randomly shuffled across the test set while all other features remain fixed, and the resulting reduction in R^2 relative to the baseline is recorded. The mean of these reductions over all repetitions is reported as the permutation importance. For simplicity, interaction terms of polynomial regression are not listed.

Based on the above listed metrics from Table 6, XGBoost is chosen to predict F_c while for F_f SVR is a good trade of between the metrics. These algorithms are suited for the regression task, which aims to capture the non-linear errors made by the simulation. The study indicates that ensemble tree-based methods are suited for this task, as they can effectively capture the nonlinear relationships between the input parameters and the process forces, while also being robust to noise in a relatively small dataset. Support Vector Regression (SVR) performed moderately well for F_f, reflecting its ability to handle nonlinear problems in low-dimensional spaces. It was noted that linear and polynomial regression mostly had a worse performance than AI approaches. In addition, out of the AI algorithms, the Neural Network performed the least favourable, as they usually require larger training sets to avoid overfitting and to exploit their ability for modelling complex nonlinearities. Linear regression performed the worst, which confirms that the relationship between cutting parameters and process forces is strongly nonlinear and cannot be captured with a linear model. With an MAE of only 5.65 N / 7.6 N over all conducted experiments and simulations for F_c and F_f, the proposed grey-box model resulted in the reduction of mean absolute error and mean squared error of 97.9 % and 99.9 % for F_c and 94.9 % and 99.7 % for F_f respectively. When determining the deviation from predicted to real modelling error and calculating the resulting error of the grey-box model to the measured forces, the mean error and standard deviation of the grey-box model is 1.3 % and 0.1 respectively. Thus, the proposed grey-box model is superior in predicting the mechanical loads over the white-box model.

In this study it became clear that even when determining the Johnson-Cook constitutive model for a metal with state of the art equipment such as a Gleeble 3800c for precise compression tests and Split-Hopkins-Pressure Bars for high strain rate material testing, the achievable accuracy of predicting mechanical loads of simulations employing this model can be further improved by a grey-box model. However, the uniqueness of the JC parameters is a clear benefit and therefore omits solving an optimization problem of the inverse identification of model parameters. Of the applied algorithms which make up the black-box part of the proposed grey-box approach, XGBoost and SVR are found to be the most precise. Although, the Neural Network features a plane which resembles the one from SVR, the predictions where the worst when comparing the mean absolute error and mean squared error. A possible cause could be the limited training dataset compared to the amount of trainable parameters. With reference to the simulated predictions of mechanical loads, it has to be noted that all grey-box models delivered better prediction results than the white-box models. The applications of linear and polynomial regression led to an increase in prediction errors over the chosen AI-algorithms, proving the advantages of the presented modelling techniques.

4. Conclusion

This study focuses on the improvement of mechanical load prediction in cutting simulations for a wide range of process parameters. The main conclusions can be drawn as follows:

- The accuracy of mechanical load prediction in metal cutting simulations using FEA heavily depends on the material model used to represent flow stress under high strain rates and temperatures. While the Johnson-Cook model is widely used, it performs poorly outside its calibration range, leading to discrepancies between simulated and measured process forces.
- To address this limitation, a grey-box modelling approach was developed by first calibrating the Johnson-Cook model for normalized AISI1045 using state of the art material testing equipment such as Split- Hopkinson pressure bar and high-temperature compression tests on a Gleeble 3800c.
- A comparison between 2D orthogonal cutting simulations and corresponding experiments across 110 test conditions revealed nonlinear discrepancies between simulated and experimentally determined process forces. Machine learning algorithms are known to capture non-linearities efficiently, which is why a grey-box framework is implemented to tackle the issue described above. The algorithms Random Forest, XGBoost, Support Vector Regression and Neural Networks were implemented alongside linear and polynomial regression.
- Supported by the lowest MAE, MSE and MAPE XGBoost captured the errors of modelled cutting forces the best, while Support Vector Regression is determined suitable for predicting these errors for the feed force. At the given task, machine learning algorithms were superior to linear and polynomial regression.
- The grey-box model achieved a mean error of 1.3 % and a standard deviation of 0.1 in cutting/feed force prediction. This demonstrates that the combination of physics-based models and data-driven models into grey-box models significantly improves prediction accuracy, even with limited data.

CRediT authorship contribution statement

Erik Krumme: Writing – original draft, Visualization, Formal analysis, Data curation. **Nithin Kumar Bandaru:** Writing – original draft, Formal analysis, Data curation. **Jan Wolf:** Writing – review & editing, Writing – original draft, Visualization, Validation, Project administration, Methodology, Investigation, Formal analysis, Data curation, Conceptualization. **Hans-Christian Möhring:** Writing – review & editing, Supervision, Project administration, Funding acquisition. **Martin Dienwiebel:** Writing – review & editing, Supervision, Funding acquisition. **Andreas Zabel:** Writing – review & editing, Supervision, Project administration, Funding acquisition.

Declaration of Competing Interest

The authors declare that they have no known competing financial interests or personal relationships that could have appeared to influence the work reported in this paper.

Acknowledgements

The scientific work has been supported by the German Research Foundation (DFG) within the research priority program SPP 2402 with project numbers 521378544 and 521377466. The authors thank the DFG for this funding and intensive technical support.

The authors would like to thank the Institute for Metal Forming Technology (IFU) of the University of Stuttgart for providing access to the Gleeble 3800c. The authors would like to express their gratitude to Paul Horn GmbH for generously providing the necessary tools.

References

[1] Ivester R, Kennedy M, Davies M, Stevenson R, Thiele J, Furness R, Athavale S. Assesment of machining models: progress report. Mach Sci Technol 2000;4:511–38. https://doi.org/10.1080/10940340008945720.

[2] Binder M, Klocke F, Lung D. Tool wear simulation of complex shaped coated cutting tools. Wear 2015:600–7. https://doi.org/10.1016/j.wear.2015.01.015.
[3] Tamizharasan T, Senthil Kumar N. Optimization of cutting inserts geometry using DEFORM-3D: Numerical simulation and experimental validation. Int J Simul Model 2012;11:65–76. https://doi.org/10.2507/IJSIMM11(2)1.200.
[4] Mourtzis D, Doukas M, Bernidaki D. Simulation in manufacturing: review and challenges. Procedia CIRP 2014;25:213–29. https://doi.org/10.1016/j.procir.2014.10.032.
[5] Storchak M, Stehle T, Möhring H-C. Numerical modeling of cutting characteristics during short hole drilling: modeling of kinetic characteristics. J Manuf Mater Process 2023;(6):195. https://doi.org/10.3390/jmmp7060195.
[6] Sadeghifar M, Sedaghati R, Jomaa W, Songmene V, Sadeghifar M, Sedaghati R, Jomaa W, Songmene V. A comprehensive review of finite element modeling of orthogonal machining process: chip formation and surface integrity predictions. Int J Adv Manuf Technol 2018;96:3747–91. https://doi.org/10.1007/s00170-018-1759-6.
[7] Zhu L, Zhu C, Pei J, Li X, Wang W. Prediction of three-dimensional milling forces based on finite element. Adv Mater Sci Eng 2014:918906. https://doi.org/10.1155/2014/918906.
[8] Soliman HA, Shash AY, El Hossainy TM, Abd-Rabou M. Investigation of process parameters in orthogonal cutting using finite element approaches. Heliyon 2020;6:e05498. https://doi.org/10.1016/j.heliyon.2020.e05498.
[9] Korkmaz ME, Gupta MK. A state of the art on simulation and modelling methods in machining: future prospects and challenges. Arch Comput Methods Eng 2023;30:161–89. https://doi.org/10.1007/s11831-022-09794-9.
[10] Klippel H, Süssmaier S, Röthlin M, Afrasiabi M, Pala U, Wegener K. Simulation of the ductile machining mode of silicon. Int J Adv Manuf Technol 2021;115:1565–78. https://doi.org/10.1007/s00170-021-07167-3.
[11] Calamaz M, Coupard D, Nouari M, Girot F. Numerical analysis of chip formation and shear localisation processes in machining the Ti-6Al-4V titanium alloy. Int J Adv Manuf Technol 2011;52:887–95. https://doi.org/10.1007/s00170-010-2789-x.
[12] Usui E, Shirakashi T, Kitagawa T. Analytical prediction of cutting tool wear. Wear 1984;100:129–51. https://doi.org/10.1016/0043-1648(84)90010-3.
[13] Duc-Toan N, Tien-Long B, Dong-Won J, Seung-Han Y, Young-Suk K. A modified johnson–cook model to predict stress-strain curves of boron steel sheets at elevated and cooling temperatures. High Temp Mater Proc 2012;31:37–45. https://doi.org/10.1515/HTMP.2011.127.
[14] Lourenço R, Andrade-Campos A, Georgieva P. The use of machine-learning techniques in material constitutive modelling for metal forming processes. metals 2022;12:427. https://doi.org/10.3390/met12030427.
[15] Chinesta F, Filice F, Micari F, Rizzuti S, Umbrello D. Assessment of material models through simple machining tests. Int J Mater Form 2009;1:507–10. https://doi.org/10.1007/s12289-008-0171-4.
[16] Andrade-Campos A, Thuillier S, Martins J, Carlone P, Tucci F, Valente R, Paulo RM, Sousa RJA de. Integrated Design in Welding and Incremental Forming: Material Model Calibration for Friction Stir Welded Blanks. Procedia Manuf 2020;47:429–34. https://doi.org/10.1016/j.promfg.2020.04.327.
[17] Zerilli FJ, Armstrong RW. Dislocation-mechanics-based constitutive relations for material dynamics calculations. J Appl Phys 1987;61:1816–25. https://doi.org/10.1063/1.338024.
[18] Li T, Zhao B, Lu X, Xu H, Zou D. A comparative study on Johnson Cook, Modified Zerilli-Armstrong, and Arrhenius-Type constitutive models to predict compression flow behavior of SnSbCu alloy. Materials 2019;12:1726. https://doi.org/10.3390/ma12101726.
[19] Iqbal SA, Mativenga PT, Sheikh MA. Characterization of machining of AISI 1045 steel over a wide range of cutting speeds. Part 2: Evaluation of flow stress models and interface friction distribution schemes. Proc Inst Mech Eng B J Eng Manuf 2007;221:917–26. https://doi.org/10.1243/09544054JEM797.
[20] Bodner SR, Partom Y. Constitutive Equations for Elastic-Viscoplastic Strain-Hardening Materials. J Appl Mech 1975;42:385–9. https://doi.org/10.1115/1.3423586.
[21] Johnson GR, Cook WH. A constitutive model and data for metals subjected to large strains, high strain rates, and high temperatures. Proc 7th Int Symp Ballist 1983:541–7.
[22] Ojal N, Cherukuri HP, Schmitz TL, Devlugt KT, Jaycox AW. A combined experimental and numerical approach that eliminates the non-uniqueness associated with the Johnson-Cook parameters obtained using inverse methods. Int J Adv Manuf Technol 2022;120:2373–84. https://doi.org/10.1007/s00170-021-08640-9.
[23] Geng P, Qin G, Zhou J, Zou Z. Hot deformation behavior and constitutive model of GH4169 superalloy for linear friction welding process. J Manuf Process 2018;32:469–81. https://doi.org/10.1016/j.jmapro.2018.03.017.
[24] Aktürk M, Boy M, Gupta MK, Waqar S, Krolczyk GM, Korkmaz ME. Numerical and experimental investigations of built orientation dependent Johnson–Cook model for selective laser melting manufactured AlSi10Mg. J Mater Res Technol 2021;15:6244–59. https://doi.org/10.1016/j.jmrt.2021.11.062.
[25] Daoud M, Chatelain JF, Bouzid A. Effect of rake angle-based Johnson-Cook material constants on the prediction of residual stresses and temperatures induced in Al2024-T3 machining. Int J Mech Sci 2017;122:392–404. https://doi.org/10.1016/j.ijmecsci.2017.01.020.
[26] Dodla S, Kirpalani Idnani KJ, Katyal A. Finite element machining simulations of aerospace materials. Mater Today Proc 2021;46:991–8. https://doi.org/10.1016/j.matpr.2021.01.136.
[27] Zhang X, Yao W, Zhu X, Hu Z, Zhu W, Huang H, Li W. Determination of Johnson–Cook constitutive of 15-5 PH steel processed by selective laser melting. Materials 2023;16:800. https://doi.org/10.3390/ma16020800.
[28] Karkalos NE, Markopoulos AP. Determination of Johnson-Cook material model parameters by an optimization approach using the fireworks algorithm. Procedia Manuf 2018;22:107–13. https://doi.org/10.1016/j.promfg.2018.03.017.
[29] Wang Y, Zeng X, Chen H, Yang X, Wang F, Zeng L. Modified Johnson-Cook constitutive model of metallic materials under a wide range of temperatures and strain rates. Results Phys 2021;27:104498. https://doi.org/10.1016/j.rinp.2021.104498.
[30] Eisseler R, Gutsche D, Maucher C, Möhring H-C. Inverse determination of Johnson-Cook parameters of additively produced anisotropic maraging steel. Materials 2021;15:26. https://doi.org/10.3390/ma15010026.
[31] Krumme E, Saelzer J, Zabel A. Fließspannung hoch dynamisch charakterisieren. maschinenbau 2024;4:10–5. https://doi.org/10.1007/s44029-024-1158-8.
[32] Kreyszig E, Kreyszig H, Norminton J. Advanced engineering mathematics. 10th ed. Hoboken: John Wiley & Sons Inc; 2011.
[33] Shokry A, Gowid S, Mulki H, Kharmanda G. On the prediction of the flow behavior of metals and alloys at a wide range of temperatures and strain rates using Johnson–Cook and modified Johnson–Cook-Based models: a review. Materials 2023;16:1574. https://doi.org/10.3390/ma16041574.
[34] Laakso SVA. Damage does not cut it – Saturated damage in FEM modelling of metal cutting breaks the simulation but not the chip. Procedia Manuf 2020;51:806–11. https://doi.org/10.1016/j-promfg.2020.10.113.
[35] Othman R. The Kolsky-Hopkinson Bar Machine: Selected Topics. 1st ed. Cham: Springer; 2018.
[36] Miyambo ME, Kallon DVV, Pandelani T, Reinecke JD. Review of the development of the split Hopkinson pressure bar. Procedia CIRP 2023;119:800–8. https://doi.org/10.1016/j.procir.2023.04.010.
[37] Ramesh KT. High Rates and Impact Experiments. In: SharpeWN, editors. Springer Handbook of Experimental Solid Mechanics. Boston: Springer; 2008. p. 929–60.
[38] Tiffe, M. 2018. Charakterisierung grundlegender Mechanismen für die Simulation der Spanbildung mithilfe der FEM. Dissertation, Dortmund.
[39] Priest J, Ghadbeigi H, Ayvar-Soberanis S, Liljerehn A, Way M. A modified Johnson-Cook constitutive model for improved thermal softening prediction of machining simulations in C45 steel. Procedia CIRP 2022;108:106–11. https://doi.org/10.1016/j.procir.2022.03.022.
[40] Ramos A, Autenrieth H, Strauß T, Deuchert M, Hoffmeister J, Schulze V. Characterization of the transition from ploughing to cutting in micro machining and evaluation of the minimum thickness of cut. J Mater Process Technol 2012;212:594–600. https://doi.org/10.1016/j.jmatprotec. 2011.07.007.
[41] Toenshoff HK. Hard Material Cutting. In. The International Academy for Production Engineering, editors. CIRP Encyclopedia of Production Engineering. Berlin, Heidelberg: Springer; 2018. p. 1–9.
[42] Spittel M, Spittel T. Steel symbol/number: C45/1.0503. In: Spittel M, Spittel T, Warlimont H, Landolt H, Börnstein R, Martienssen W, editors. Numerical data and functional relationships in science and technology: New series. Berlin: Springer; 2009. p. 210–5.
[43] Spriggs GE. 4 Properties of hardmetals and cermets. In: Beiss P, Ruthardt R, Warlimont H, Leichtfried G, Landolt H, Börnstein R, Martienssen W, Madelung O, editors. Numerical data and functional relationships in science and technology: New series, 13. Berlin: Springer; 2002. p. 86–117.
[44] Martan J, Beneš P. Thermal properties of cutting tool coatings at high temperatures. Thermochim Acta 2012;539:52–5. https://doi.org/10.1016/j.tca.2012.03.029.
[45] Zhao J, Liu Z, Wang B, Hu J. PVD AlTiN coating effects on tool-chip heat partition coefficient and cutting temperature rise in orthogonal cutting Inconel 718. Int J Heat Mass Transf 2020;163:120449. https://doi.org/10.1016/j.ijheatmasstransfer.2020.120449.
[46] Shi B, Attia H. Current status and future direction in the numerical modeling and simulation of machining processes: A critical literature review. Mach Sci Technol 2010;14:149–88. https://doi.org/10.1080/10910344.2010.503455.
[47] Takeishi N, Kalousis A. Deep Grey-Box Modeling With Adaptive Data-Driven Models Toward Trustworthy Estimation of Theory-Driven Models. Proc 26th Int Conf Artif Intell Stat 2023;206:4089–100.
[48] Menesklou P, Sinn T, Nirschl H, Gleiss M. Grey box modelling of decanter centrifuges by coupling a numerical process model with a neural network. minerals 2021;11:755. https://doi.org/10.3390/min11070755.
[49] Reeber T, Wolf J, Möhring H-C. A data-driven approach for cutting force prediction in FEM machining simulations using gradient boosted machines. J Manuf Mater Process 2024;8:107. https://doi.org/10.3390/jmmp8030107.
[50] Breiman L. Random forests. Mach Learn 2001;45:5–32. https://doi.org/10.1023/A:1010933404324.
[51] Biau G. Analysis of a random forests model. J Mach Learn Res 2012;13:1063–95. https://doi.org/10.48550/arXiv.1005.0208.
[52] Jonssnon, E., Fredrikson, S. 2021. An Investigation of How Well Random Forest Regression Can Predict Demand, ⟨https://www.diva-portal.org/smash/get/diva2:1594694/FULLTEXT01.pdf⟩; [accessed 12 January 2025].
[53] Couronné R, Probst P, Boulesteix A-L. Random forest versus logistic regression: a large-scale benchmark experiment. BMC Bioinforma 2018;19:270. https://doi.org/10.1186/s12859-018-2264-5.
[54 Sabzekar M, Hasheminejad S. Robust regression using support vector regressions. Chaos Solitons Fractals 2021;144:110738. https://doi.org/10.1016/j.chaos.2021.110738.
[55] Agustina SD, Mustakim O, Bella C, Ramadhan MA. Support Vector Regression Algorithm Modeling to Predict the Availability of Foodstuff in Indonesia to Face

the Demographic Bonus. J Phys Conf Ser 2018;1028:012240. https://doi.org/10.1088/1742-6596/1028/1/012240.
[56] Smola AJ, Schölkopf B. A tutorial on support vector regression. Stat Comput 2004;14:199–222. https://doi.org/10.1023/B:STCO.0000035301.49549.88.
[57] Chen T, Guestrin C. XGBoost: A Scalable Tree Boosting System. Proc 22nd ACM SIGKDD Int Conf Knowl Discov Data Min 2016;11:785–94. https://doi.org/10.1145/2939672.2939785.
[58] Sheng C, Yu H. An optimized prediction algorithm based on XGBoost. Int Conf Netw Netw Appl (NaNA) 2022 2022:1–6. https://doi.org/10.1109/NaNA56854.2022.00082.
[59] Mehlig B. Machine Learning with Neural Networks: An Introduction for Scientists and Engineer. 1st ed. Cambridge: Cambridge University Press; 2021.
[60] Sirigiri VKR, Gudiga VY, Gattu US, Suneesh G, Buddaraju KM. A review on Johnson Cook material model. Mater Today Proc 2022;62:3450–6. https://doi.org/10.1016/j.matpr.2022.04.279.
[61] Khare S, Kumar K, Choudhary S, Singh PK, Verma RK, Mahajan P. Determination of Johnson–Cook material parameters for armour plate Using DIC and FEM. Met Mater Int 2021;27:4984–95. https://doi.org/10.1007/s12540-020-00895-3.
[62] Wolf J, Bandaru NK, Dienwiebel M, Möhring H-C. A novel grey-box based friction model for a wide range of machining conditions. Wear 2025;580:206295. https://doi.org/10.1016/j.wear.2025.206295.
[63] Laakso SVA, Agmell M, Stahl J-C. The mystery of missing feed force — The effect of friction models, flank wear and ploughing on feed force in metal cutting simulations. J Manuf Process 2018;33:268–77. https://doi.org/10.1016/j.jmapro.2018.05.024.